

XPBD: Position-Based Dynamics with Smoothing Kernels Handles Continuum Inelasticity

CHANG YU*, UCLA, USA

XUAN LI*, UCLA, USA

LEI LAN, University of Utah, USA

YIN YANG, University of Utah, USA

CHENFANFU JIANG, UCLA, USA

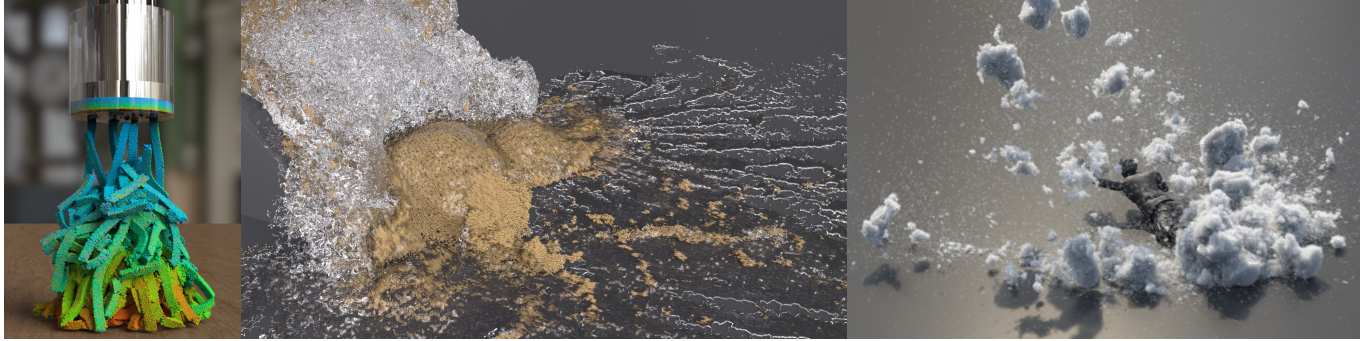


Fig. 1. XPBD supports simulating a wide range of classical continuum elastoplastic material models such as Von-Mises plasticine, Drucker-Prager sand, and Cam Clay snow, as well as their interactions with traditional PBD materials such as Position-based Fluid.

Position-based Dynamics (PBD) and its extension, eXtended Position-based Dynamics (XPBD), have been predominantly applied to compliant constrained elastodynamics, with their potential in finite strain (visco-) elastoplasticity remaining underexplored. XPBD is often perceived to stand in contrast to other meshless methods, such as the Material Point Method (MPM). MPM is based on discretizing the weak form of governing partial differential equations within a continuum domain, coupled with a hybrid Lagrangian-Eulerian method for tracking deformation gradients. In contrast, XPBD formulates specific constraints, whether hard or compliant, to positional degrees of freedom. We revisit this perception by investigating the potential of XPBD in handling inelastic materials that are described with classical continuum mechanics-based yield surfaces and elastoplastic flow rules. Our inspiration is that a robust estimation of the velocity gradient is a sufficiently useful key to effectively tracking deformation gradients in XPBD simulations. By further incorporating implicit inelastic constitutive relationships, we introduce a plasticity in-the-loop updated Lagrangian augmentation to XPBD. This enhancement enables the simulation of elastoplastic, viscoplastic, and granular substances following their standard constitutive laws. We demonstrate the effectiveness of our method through high-resolution and real-time simulations of diverse materials such as snow, sand, and plasticine, and its integration with standard XPBD simulations of cloth and water.

CCS Concepts: • **Computing methodologies** → **Physical simulation**.

Additional Key Words and Phrases: position-based dynamics, material point method, continuum mechanics, elastoplasticity, viscoplasticity

*Both authors contributed equally to this research.

Authors' addresses: Chang Yu, g1n0st@live.com, UCLA, Los Angeles, California, USA; Xuan Li, xuan.shayne.li@gmail.com, UCLA, Los Angeles, California, USA; Lei Lan, lanlei.virhum@gmail.com, University of Utah, Salt Lake City, Utah, USA; Yin Yang, yangzzzy@gmail.com, University of Utah, Salt Lake City, Utah, USA; Chenfanfu Jiang, chenfanfu.jiang@gmail.com, UCLA, Los Angeles, California, USA.

1 INTRODUCTION

Position-based Dynamics (PBD) [Müller et al. 2007] and its extension eXtended Position-based Dynamics (XPBD) [Macklin et al. 2016] are widely adopted in compliant constrained dynamics, particularly favored for their performance and simplicity for graphics applications such as rigid bodies [Müller et al. 2020], soft bodies [Bender et al. 2014], cloth [Müller et al. 2007], rods [Umetani et al. 2015] and hair [Müller et al. 2012]. When simulating mesh-based elasticity, it is straightforward to model XPBD constraints with FEM hyperelastic energies defined over explicit mesh topology. This allows for effective simulations of elasticity while maintaining the stability and speed of XPBD. For example, quadratic energy potentials [Chen et al. 2023] can be formulated using XPBD-style constraints. Macklin and Müller [2021] and Ton-That et al. [2023] reformulated stable Neo-Hookean [Smith et al. 2018] to demonstrate XPBD's capability in handling nonlinear elasticity.

For inelasticity, on the other hand, two significant challenges emerge. Firstly, topology changes during material splitting and merging introduce great complexity in maintaining a high quality mesh, often necessitating remeshing. Secondly, while there have been explorations that enhances Position-based Fluids (PBF) [Macklin and Müller 2013] with the conformation tensor [Barreiro et al. 2017] for viscoelastic fluids, it remains underexplored for XPBD to model physically-grounded finite strain (visco-) elastoplastic constitutive laws from classical continuum mechanics, such as von-Mises [Mises 1913], Drucker-Prager [Drucker and Prager 1952] and Herschel-Bulkley [Herschel and Bulkley 1926] flow rules. Being able to simulate them would greatly improve XPBD's versatility and intuitive controllability of material parameters.

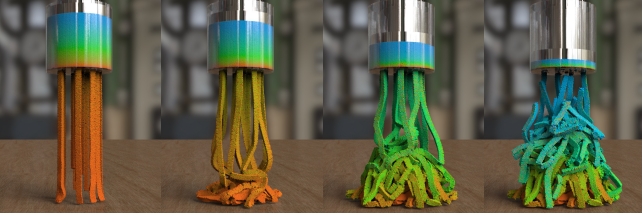


Fig. 2. **Noodles.** We simulate noodles modeled using Von Mises plasticity as it is pressed through a cylindrical mold.

In comparison with XPBD’s success in mesh-based materials, Material Point Method (MPM)’s development in graphics over the past decade has majorly focused on inelastic phenomena with topology change. MPM is based on the weak form of governing PDEs and employs a hybrid Lagrangian-Eulerian approach for spatial discretization. It handles topology changes, self collision, and finite strain deformation without overhead, and thus has been used for many continuum inelastic phenomena such as snow [Stomakhin et al. 2013], lava [Stomakhin et al. 2014], sand [Klár et al. 2016], mud [Tampubolon et al. 2017], metal [Wang et al. 2020], foam [Ram et al. 2015], and fracture [Wolper et al. 2019]. While substantial progress has been made in these areas, MPM exhibits several notable drawbacks, including excessive numerical dissipation due to particle-grid transfers [Jiang et al. 2015], artificial stickiness that hampers material separation [Fei et al. 2021], and resolution-dependent gaps between colliding materials [Jiang et al. 2017]. None of these issues are present in XPBD. This raises a natural question: *Can we simulate MPM-style phenomena using XPBD instead?*

Towards addressing this question, we make an important observation: the primary factor that facilitates the modeling of inelasticity lies not in the hybrid Lagrangian-Eulerian nature of MPM, but rather in its use of an updated Lagrangian formulation for the deformation gradient tensor. In particular, one considers the time $n + 1$ velocity \mathbf{v}^{n+1} to be defined over the previous time n domain Ω^n through the Lagrangian velocity \mathbf{V} of a particle traced back using the inverse deformation map $\phi^{-1}(\mathbf{x}, t): \mathbf{v}^{n+1}(\mathbf{x}) = \mathbf{V}(\phi^{-1}(\mathbf{x}, t^n), t^{n+1})$ [Jiang et al. 2016], where t represents the continuous time variable. This enables the derivation of the rate form of the deformation gradient \mathbf{F} given by $\dot{\mathbf{F}} = (\nabla \mathbf{v})\mathbf{F}$, which can be further discretized into $\mathbf{F}^{n+1} = (\mathbf{I} + \Delta t \nabla \mathbf{v}^{n+1})\mathbf{F}^n$, where Δt is the time step size, allowing one to track the deformation gradient *without referring to a material space configuration*.

Inspired by this observation, if we can track the deformation gradient tensor \mathbf{F} using an updated Lagrangian view in XPBD, then

Table 1. XPBI keeps PBD’s pure particle nature of the Degrees of Freedom while allowing MPM-style plasticity and granular material modeling through an updated Lagrangian treatment of the deformation and classical continuum mechanics-based elastoplastic flow rules.

	Lagrangian	DOF	Plasticity	Granular
MPM	Updated	Grid	Flow Rule	Continuum
PBD	Total	Particle	N/A	Sphere Approx.
Ours	Total & Updated	Particle	Flow Rule	Continuum

by treating \mathbf{F} as a function of XPBD degrees of freedom, we can modify XPBD to resemble a “material point” approach. As detailed in later sections, this task reduces to robustly computing and differentiating the velocity gradient tensor. We present developments surrounding these ideas by introducing eXtended Position-based Inelasticity (XPBI), where the X represents not only the incorporation of XPBD augmentation but also the use of velocity as the primal variable. This approach computes the updated Lagrangian deformation gradient using a velocity-based formulation, allowing us to handle various inelastic effects. Using velocities as primary variables allows for direct evaluation of the velocity gradient and particle-wise constraints using interpolation kernels defined at t^n , aligning with standard MPM practices, while using positions could introduce uncertainties in updating kernels during implicit iterations. By further incorporating an implicit plasticity treatment and additional stability-enhancing components, our method leverages the efficiency and simplicity of PBD while capturing the complex inelastic material responses typically associated with MPM; see Table. 1. In summary, our contributions include:

- An updated Lagrangian augmentation for XPBD that tracks meshless deformation gradients and per-particle constraints;
- XPBI, a fully implicit plasticity-aware algorithm capable of handling continuum mechanics-based elastoplastic/viscoplastic laws;
- An investigation for practical stability enhancements, such as XSPH and position correction, and validations of our method with various practical examples.

2 RELATED WORK

Inelasticity with PBD. Müller et al. [2007] introduced PBD, which replaces internal forces with positional constraints and produces appealing, stable and real-time simulations. Its first-order convergence was studied by Plunder and Merino-Aceituno [2023]. XPBD [Macklin et al. 2016], an extension of PBD, utilizes the compliant-constraint framework [Tournier et al. 2015] to uniformly handle soft and hard constraints to simulate elasticity. Our work follows the latest XPBD paradigm [Macklin et al. 2019] with substeps. Other PBD materials include rigid body [Müller et al. 2020], soft body [Bender et al. 2014], cloth [Müller et al. 2007], hair [Müller et al. 2012], elastic rod [Umetani et al. 2015], sand [Macklin et al. 2014], fluid [Macklin and Müller 2013] with surface tension [Xing et al. 2022] and their unified couplings [Abu Rumman et al. 2020; Frâncu and Moldoveanu 2017; Macklin et al. 2014]. We refer to Bender et al. [2017] for a comprehensive survey.

For *continuum* materials, Bender et al. [2014] defined a constraint for the elastic strain energy. Müller et al. [2015] constrained the strain tensor directly instead. Macklin and Müller [2021] reformulated stable Neo-Hookean using XPBD. Plastic deformation and fracture can be modeled by shape matching [Chentanez et al. 2016; Falkenstein et al. 2017; Jones et al. 2016], prioritizing efficiency over accuracy. Macklin et al. [2014] simulated sand as colliding spheres with friction. SideFX Houdini’s Vellum PBD solver further added spring-like cohesion for snow. Without further utilizing continuum mechanics-based inelastic models, these approaches have limited mechanical intuition and physical parameter controllability. A step

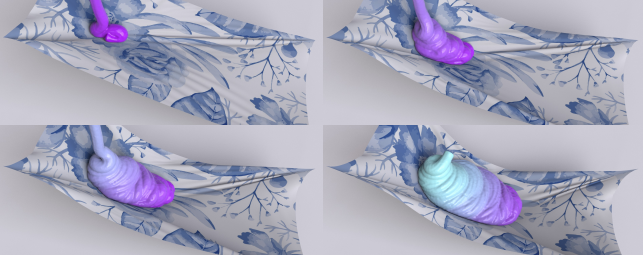


Fig. 3. **Cloth.** XPBD fits into traditional XPBD pipeline and naturally couples updated Lagrangian materials (viscoplastic paint) and mesh-based geometry (cloth).

forward was proposed by Barreiro et al. [2017], which enhances PBF with the conformation tensor for viscoelastic fluids. Nevertheless, it does not incorporate finite strain continuum mechanics, limiting its suitability in modeling general elastoplastic and viscoplastic laws.

Inelasticity with MPM. MPM was introduced by Sulsky et al. [1994] as a hybrid Lagrangian/Eulerian approach for solids. Since its adoption in graphics [Hegemann et al. 2013; Stomakhin et al. 2013], MPM has gained significant attentions for its automatic topology change and material versatility. Snow plasticity was first done by projecting principal stretches [Stomakhin et al. 2013]. Phase change was modeled by [2014] through a dilational/deviatoric splitting of the constitutive model. Yue et al. [2015] adopted Herschel-Bulkley viscoplasticity for foam. Ram et al. [2015] used the Oldroyd-B model for viscoelastic fluids. Fei et al. [2019] developed an analytical plastic flow approach for shear-dependent liquids. Following Drucker-Prager yield criterion, Daviet and Bertails-Descoubes [2016]; Klár et al. [2016] modeled sand as continuum granular materials and Tampubolon et al. [2017] further added wetting. Wolper et al. [2020, 2019] captured dynamic fracture using Non-Associated Cam-Clay (NACC) plasticity and damage mechanics. Advocating implicit integrators, stiff plastic materials like metal was simulated with Newton-Krylov MPM [Wang et al. 2020], while Fang et al. [2019] used Alternating Direction Methods of Multipliers (ADMM) for viscoelasticity and elastoplasticity and Li et al. [2022] proposed a variational implicit inelasticity formulation.

Inelasticity with Other Discretizations. Smoothed Particle Hydrodynamics (SPH) was originally developed for simulating incompressible flow. Clavet et al. [2005] added dynamic-length springs for viscoelasticity. Jones et al. [2014] and Müller et al. [2004] solved Moving Least Squares (MLS) for elastoplasticity. Gerszewski et al. [2009] first used deformation gradient tensor with multiplicative elastoplastic decomposition in SPH. Alduán and Otaduy [2011] and Yang et al. [2017] modeled granular materials based on Drucker-Prager yielding. Takahashi et al. [2015] used an implicit SPH formulation to simulate viscous fluids. Gissler et al. [2020] developed an implicit SPH snow solver similarly to Stomakhin et al. [2013]’s MPM treatment. Using power diagram-based particle-in-cell [Qu et al. 2022] and MLS-MPM [Hu et al. 2018], power plastics [Qu et al. 2023] simulated inelastic flow with an XPBD-style Gauss-Seidel solver. Peridynamics [Silling 2000] defines pairwise forces and integrates particle interactions. He et al. [2017] combined peridynamics

with projective dynamics [Bouaziz et al. 2014] and modeled Drucker-Prager plasticity. Chen et al. [2018] used isotropic linear elasticity with plasticity and simulated fracture.

3 METHOD

We start with briefly reviewing XPBD [Macklin et al. 2016], which lets hyperelasticity be governed by Newton’s equations of motion through a potential $U(\mathbf{x})$: $\mathbf{M}\ddot{\mathbf{x}} = -\nabla U^T(\mathbf{x})$, where \mathbf{M} is the mass matrix and $\mathbf{x} = [x_1, x_2, \dots, x_p]^T$ is the unknown position states. XPBD assumes $U(\mathbf{x})$ can be further expressed as $U(\mathbf{x}) = \frac{1}{2}\mathbf{C}(\mathbf{x})^T \mathbf{a}^{-1} \mathbf{C}(\mathbf{x})$, where $\mathbf{C} = [C_1(\mathbf{x}), C_2(\mathbf{x}), \dots, C_m(\mathbf{x})]^T$ contains m constraints, and \mathbf{a} is a diagonal compliance matrix. The elastic internal force \mathbf{f} and Lagrange multiplier λ are then shown to be

$$\mathbf{f} = -\nabla \mathbf{C}(\mathbf{x})^T \mathbf{a}^{-1} \mathbf{C}(\mathbf{x}), \quad (1)$$

$$\lambda = -\tilde{\mathbf{a}}^{-1} \mathbf{C}(\mathbf{x}). \quad (2)$$

where $\tilde{\mathbf{a}} = \frac{\mathbf{a}}{\Delta t^2}$ and Δt is the time step size.

3.1 Rewriting StVK Elasticity as Constraints

For modeling elasticity, we adopt the St. Venant-Kirchhoff (StVK) model with Hencky strains. As in Klár et al. [2016], Gao et al. [2017], the advantage of this choice is for math/code simplicity and runtime efficiency – it allows return mapping to have analytical solutions for certain plastic flows, eliminating the need for numerical solutions. The elastoplastic behavior of isotropic materials is characterized in the principal stretch space Σ via singular value decomposition (SVD) [Stomakhin et al. 2012] of the deformation gradient \mathbf{F} . The element’s total potential energy Φ can be expressed as $\Phi = V^0 \Psi$, where V^0 is an element’s rest volume and Ψ is the energy density, assuming piecewise constant element deformations, i.e., one particle has one deformation gradient. For StVK we have energy density Ψ

$$\Psi = \mu \text{tr} \left(\log(\Sigma)^2 \right) + \frac{\lambda}{2} (\text{tr}(\log(\Sigma)))^2, \quad (3)$$

where μ and λ are the Lamé parameters.

To convert Φ into constraints, our first option is to separately handle each term. As done by Macklin and Müller [2021] for Neo-Hookean, by utilizing $\Phi = \frac{1}{2} \frac{1}{\alpha} C^2$, we could define two constraints for the μ and λ term respectively as

$$\alpha_\mu = 1/(2\mu V^0), \text{ and } C_\mu = \sqrt{\text{tr}(\log(\Sigma)^2)}; \quad (4)$$

$$\alpha_\lambda = 1/(\lambda V^0), \text{ and } C_\lambda = \text{tr}(\log(\Sigma)). \quad (5)$$

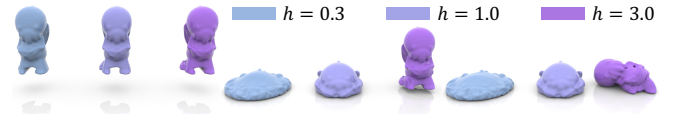


Fig. 4. XPBD simulates Herschel-Bulkley shear thinning ($h = 0.3$), viscoplastic ($h = 1.0$), and shear thickening materials ($h = 3.0$), where h controls a power law flow rate detailed in [Yue et al. 2015].



Fig. 5. **Candy Camponotus**. We simulate the brittle fracture of a candy shaped like a camponotus falling onto the ground.

Alternatively, as done by Qu et al. [2023] on power diagrams, we can absorb Lamé parameters from α to C and define a single F -dependent constraint through $\Phi = V^0 \Psi(F) = \frac{1}{2\alpha} C(F)^2$ to achieve

$$\alpha = 1/V^0, \text{ and } C(F) = \sqrt{2\Psi(F)}, \quad (6)$$

which clearly halves the number of constraints by allowing more nonlinearity in each $C(F(x))$. In practice we find both options effective, and adopt the single-constraint version for efficiency.

3.2 Gradient is All You Need

Unlike mesh-based representations [Macklin and Müller 2021] which use linear FEM to model the deformation map $\mathbf{x} = \boldsymbol{\phi}(\mathbf{X}, t)$ and compute deformation gradient $\mathbf{F} = \partial\boldsymbol{\phi}(\mathbf{X}, t)/\partial\mathbf{X}$ using an undeformed reference state $\mathbf{X} \in \Omega^0$, meshless inelastic materials cannot utilize simplex elements due to extreme deformation. We follow Jiang et al. [2016] and Gissler et al. [2020] to derive the time rate of the deformation gradient:

$$\frac{\partial}{\partial t} \mathbf{F}(\mathbf{X}, t) = \frac{\partial}{\partial t} \frac{\partial \boldsymbol{\phi}}{\partial \mathbf{X}}(\mathbf{X}, t) = \frac{\partial \mathbf{v}}{\partial \mathbf{x}}(\boldsymbol{\phi}(\mathbf{X}, t), t) \frac{\partial \boldsymbol{\phi}}{\partial \mathbf{X}}(\mathbf{X}, t), \quad (7)$$

with $\mathbf{V}(\mathbf{X}, t) = \partial\boldsymbol{\phi}(\mathbf{X}, t)/\partial t$ being the Lagrangian velocity whose Eulerian counterpart is $\mathbf{v}(\mathbf{x}, t) = \mathbf{V}(\boldsymbol{\phi}^{-1}(\mathbf{x}, t), t)$. With time discretization from t^n to t^{n+1} and the assumption that the velocity \mathbf{v} at time t^{n+1} being $\mathbf{v}^{n+1}(\mathbf{x})$ for $\mathbf{x} \in \Omega^n$, we have

$$\frac{\partial}{\partial t} \mathbf{F}(\mathbf{X}, t^{n+1}) = \frac{\partial \mathbf{v}^{n+1}}{\partial \mathbf{x}}(\boldsymbol{\phi}(\mathbf{X}, t^n)) \mathbf{F}(\mathbf{X}, t^n). \quad (8)$$

Taking $\frac{\partial}{\partial t} \mathbf{F}_p(\mathbf{X}_p, t^{n+1}) \approx (\mathbf{F}_p^{n+1} - \mathbf{F}_p^n)/\Delta t$ for a particle \mathbf{X}_p we get

$$\mathbf{F}_p^{n+1} = \mathbf{F}_p^n + \Delta t \frac{\partial \mathbf{v}^{n+1}}{\partial \mathbf{x}}(\mathbf{x}_p^n) \mathbf{F}_p^n = \left(\mathbf{I} + \Delta t \frac{\partial \mathbf{v}^{n+1}}{\partial \mathbf{x}}(\mathbf{x}_p^n) \right) \mathbf{F}_p^n \quad (9)$$

as the evolution of \mathbf{F}_p^{n+1} given \mathbf{v}^{n+1} and \mathbf{F}_p^n . With updated Lagrangian [2020], the reference space is thus always Ω^n and there is no need to store Ω^0 ; see Fig. 6. Therefore, to express constraints as functions of positions $C(\mathbf{F}(\mathbf{v}^{n+1}(\mathbf{x}^{n+1})))$, robustly estimating $\partial \mathbf{v}/\partial \mathbf{x}$ ($\forall \mathbf{x} \in \Omega^n$) and its derivative is all one needs.

Accurately estimating meshless velocity gradients is generally challenging. Most meshless shape functions require a dense neighborhood to fulfill the kernel's normalization condition. Known as neighborhood deficiency, significant accuracy degradation would occur especially for first-order derivatives (such as velocity gradient) in sparse regions. Kernel gradient correction [Bonet and Lok 1999] and the reproducing kernel particle method [Liu et al. 1995] are examples of strategies for mitigating this problem. Here, we adopt Wendland kernels [Wendland 1995] for the standard SPH kernel W and ∇W and the reweighting-based kernel gradient correction

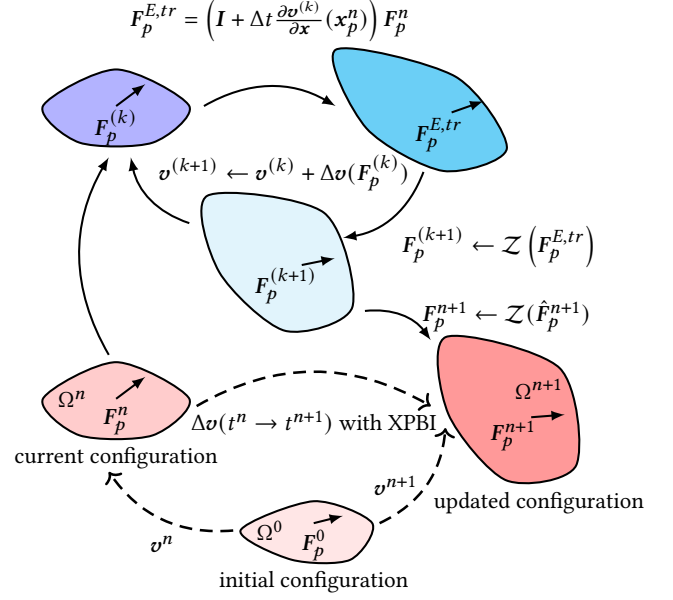


Fig. 6. **Deformation Gradient Evolution**. The dotted line (bottom) illustrates the evolution of the deformation gradient in the updated Lagrangian view, transitioning from \mathbf{F}_p^0 (initial configuration) to \mathbf{F}_p^{n+1} (updated configuration), with \mathbf{F}_p^n (current configuration) serving as the reference state. This facilitates tracking large deformations. The solid line loop (top) depicts iterations of our XPBD algorithm to simulate $t^n \rightarrow t^{n+1}$, alternating between an XPBD iteration and a fixed point iteration. During iteration k , $\mathbf{F}_p^{E,tr}$ is first estimated based on the current gradient of $\mathbf{v}^{(k)}$ (§ 3.2). Then, plasticity is applied through projection to obtain $\mathbf{F}_p^{(k+1)}$ (§ 3.3), and finally, $\mathbf{v}^{(k+1)}$ is updated by solving constraints (§ 4.1).

[Bonet and Lok 1999]. The correction matrix L_p is defined as

$$L_p = \left(\sum_b V_b^n \nabla W_b(\mathbf{x}_p) \otimes (\mathbf{x}_b - \mathbf{x}_p) \right)^{-1}, \quad (10)$$

with SVD based pseudo inverse $\mathbf{A}^{-1} = \mathbf{V} \boldsymbol{\Sigma}^{-1} \mathbf{U}^T$ to avoid singularities when calculating ill-conditioned matrix inverses for numerical stability, where $V_b^n = V_b^0 \det(\mathbf{F}_b^n)$ is the time n volume of the neighborhood particle b . As in many SPH methods, the correction is indispensable for maintaining simulation stability. See Westhofen et al. [2023] for discussions of similarly viable gradient estimation choices. Our discrete velocity gradient at particle p in Ω^n is then

$$\frac{\partial \mathbf{v}}{\partial \mathbf{x}}(\mathbf{x}_p^n) = \sum_{b \neq p} V_b^n (\mathbf{v}_b - \mathbf{v}_p) \left(L_p \nabla W_b(\mathbf{x}_p^n) \right)^T, \quad (11)$$

which is also adopted in Gissler et al. [2020]. Combining the gradient estimation with Eq. 9 and differentiating per-particle constraint $C_p(\mathbf{F}_p)$ (Eq. 6) reveals

$$\nabla_{\mathbf{x}_b} C_p|_{b \neq p} = V_b^n \frac{\partial C_p}{\partial \mathbf{F}_p} \mathbf{F}_p^{nT} (L_p \nabla W_b(\mathbf{x}_p^n)), \quad (12)$$

$$\nabla_{\mathbf{x}_p} C_p = - \sum_{b \neq p} \nabla_{\mathbf{x}_b} C_p, \quad (13)$$



Fig. 7. **Dam Breach.** Our method can be seamlessly coupled with PBF [Macklin and Müller 2013] to simulate sand and water mixture.

which provides us all necessary constraint derivatives in XPBD.

3.3 Implicit Plasticity

Plasticity in continuum mechanics is typically solved with return mapping, denoted as $\mathcal{Z}(\cdot)$, which adjusts strains according to a plastic flow rule. It projects an elastic predictor $F^{E,tr}$ onto the yield surface to ensure an inequality constraint on the stress.

To make plasticity implicit, we propose to alternate between (1) an XPBD iteration with a projected stress and (2) a stress projection. This is essentially a fixed point iteration similarly to Li et al. [2022]:

$$F_p^{(k+1)} \leftarrow \mathcal{Z}\left(F_p^{E,tr}\left(v^{(k)}\left(F_p^{(k)}\right)\right)\right), \quad (14)$$

where $F_p^{E,tr}$ is the trial elastic deformation gradient and $v^{(k)}(F_p^{(k)})$ is the updated velocity by previous k XPBD iterations based on $F_p^{(k)}$ in the previous iteration. In contrast to Li et al. [2022]’s fixed point iteration on \mathcal{Z} which functions as an independent outer loop of a full Newton optimization, our design establishes a fixed point on F , updating variables directly impacted by the fixed point iteration *within* XPBD iterations; see Fig. 6 top and Alg. 1. Resultingly, our implicit plasticity treatment introduces negligible extra cost on top of what implicit elasticity already necessitated.

Nonetheless, convergence in fixed-point iterations depends on an initial guess sufficiently close to the solution, among other conditions of the implicit function. In this paper, we do not monitor quantitative plasticity convergence since few XPBD iterations are needed for visually plausible results. We do emphasize the importance of implicit plasticity and compare it with a semi-implicit treatment which only applies plasticity at the end of a time step; see § 5.1.

4 ALGORITHM

Here we detail the XPBI pipeline and its seamlessly integration into existing XPBD. Our pseudocode for advancing a time step using velocity-based XPBD is summarized in Alg. 1.



Fig. 8. **Hourglass.** Sand in hourglass accumulates at the bottom. The material is modeled with Drucker-Prager plasticity [Klár et al. 2016].

4.1 Algorithm Overview

Similarly to MPM, we use material particles to discretize the continuum. Each particle p is governed by a constitutive model-induced constraint C_p (Eq. 6) and a plastic return mapping operator \mathcal{Z} . We use C_p to denote particle-wise inelasticity constraints ($|\{p\}| = N = \# \text{ particles}$) and C_i to denote traditional PBD constraints ($|\{i\}| = M = \# \text{ number of all other constraints}$).

Due to our dependency on velocity gradients, it is more natural to reparametrize XPBD with velocities rather than positions as primary unknown variables. Closely resembling position-based XPBD, we solve for velocities v^{n+1} and Lagrange multipliers λ^{n+1} that satisfies

$$M(v^{n+1} - \tilde{v}^n) - \nabla C(v^{n+1})^T \lambda^{n+1} = 0, \quad (15)$$

$$C(v^{n+1}) + \tilde{a} \lambda^{n+1} = 0, \quad (16)$$

by updating per-particle inelastic constraint C_p ’s corresponding Lagrangian multiplier λ_p with

$$\Delta \lambda_p = \frac{-C_p - \tilde{\alpha}_p \lambda_p}{\sum_{b=1}^N \frac{1}{m_b} |\nabla_{x_b} C_p(x)|^2 + \tilde{\alpha}_p}, \quad (17)$$

where $\alpha_p = 1/V_p^0$ and $\tilde{\alpha}_p = \alpha_p / \Delta t^2$. The velocity update is given by:

$$\Delta v = \left(M^{-1} \nabla C(x)^T \Delta \lambda \right) / \Delta t. \quad (18)$$

The velocities and multipliers are jointly updated by a colored Gauss-Seidel iteration (see § 4.3 and Alg. 1):

$$\lambda_p^{(k+1)} \leftarrow \lambda_p^{(k)} + \Delta \lambda_p, \quad v^{(k+1)} \leftarrow v^{(k)} + \Delta v. \quad (19)$$

Note that by selecting velocities as our primary unknown variables, our deformation gradient update (as derived in Eq. 8 and Eq. 9) within the Gauss-Seidel iteration allows us to directly evaluate the velocity gradient and particle-wise constraints in Ω^n using interpolation kernels defined at t^n , aligning with a typical MPM approach [Jiang et al. 2016]. Conversely, using positions as primary variables could introduce uncertainties regarding whether to update the kernels during implicit iterations, which is an intriguing area for future exploration. For collisions with standard PBD materials,

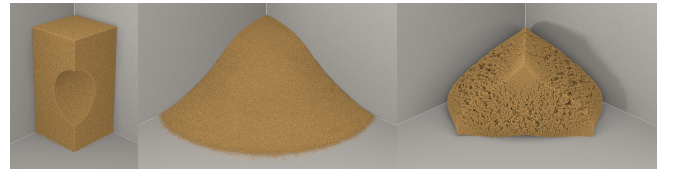


Fig. 9. Comparison on notched sand block fall. Initial (left), our fully implicit treatment (middle), and semi-implicit plasticity (right).

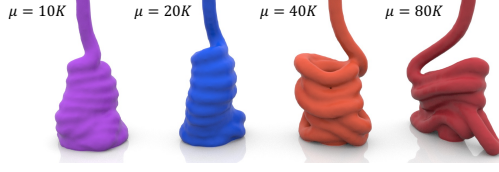


Fig. 10. XPBI effectively captures viscoplastic coiling; as the shear modulus μ increases from left to right, coils become more elastic.

as illustrated in the loop over C_i in Alg. 1, we follow the standard PBD approach, where constraints are directly evaluated using collision kernels defined by the latest candidate positions during the iterations, ensuring accurate prediction of potential collisions.

4.2 Particle Neighbor Search

We reconstruct the neighbor information for each particle at the beginning of each timestep, similarly to Macklin and Müller [2013]. A comprehensive overview of CPU- and GPU-based neighborhood search methods is surveyed by Ihmsen et al. [2014]. Each material particle is assigned the same kernel radius in our discretization scheme. We adopt a uniform spatial-grid-based method for neighborhood searches following Hoetzlein [2014]. Particles are spatially stored in cells while neighbor lists $\mathcal{N}_p = \{b \mid \|x_p - x_b\|_2 \leq k\}$ are determined by querying adjacent grid cells using the Wendland kernel's support radius $k = 2r$, and r is the SPH particle kernel radius. In addition to the total number of particles $N = |\{p\}|$, the total number of particle neighbors $\sum |\mathcal{N}_p|$ is also critical for performance, as it determines the complexity of calculating inelastic constraints. We summarize the statistics for $\sum |\mathcal{N}_p|$ in Table. 2.

4.3 Colored Gauss-Seidel

Original PBD and XPBD frameworks solve constraints iteratively using nonlinear Gauss-Seidel [Macklin et al. 2016, 2014; Müller et al. 2007]. In contrast, Macklin and Müller [2013] adopted a Jacobi-style iteration for fluids, solving each constraint independently to enhance parallelism. We found that for high resolution and often high stiffness simulations considered in this paper, Jacobi iterations too slowly propagate information and often suffer from non-convergence (also noted by Macklin et al. [2014]). Thus we implement colored Gauss-Seidel to maximize convergence, parallelism, and GPU throughput. We assign particles into cells with $\Delta x = 2r$

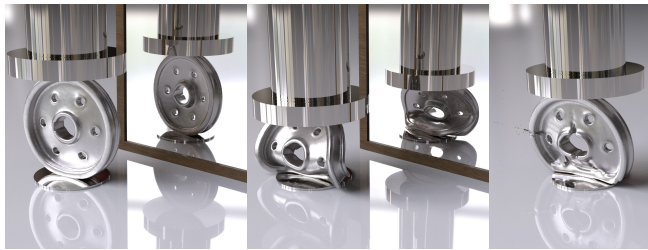


Fig. 11. Hydraulic test on a stiff aluminum wheel: initial (left), w/ (middle) and w/o (right) position correction. The simulation suffers from artificial fracture and instability without our correction.

Algorithm 1 Simulating $t^n \rightarrow t^{n+1}$ with XPBI

```

Neighbor search using  $\mathbf{x}^n$                                 ▶ § 4.2
Evaluate kernel gradient correction  $L_p$                   ▶ § 3.2
 $\mathbf{v} \leftarrow \mathbf{v}^n + \Delta t \mathbf{M}^{-1} \mathbf{f}_{\text{ext}}$ 
 $\lambda = 0$ 
for number of XPBD iterations do
  for all  $p \in \{C_p\}$  looping with colored Gauss-Seidel ▶ § 4.3 do
     $(\nabla \mathbf{v})_p \leftarrow \text{evaluateVelocityGradient}(\mathbf{x}_p^n, \mathbf{v}_p)$  ▶ § 3.2
     $\mathbf{F}_p \leftarrow (\mathbf{I} + \Delta t (\nabla \mathbf{v})_p) \mathbf{F}_p^n$ 
     $\mathbf{F}_p \leftarrow \mathcal{Z}(\mathbf{F}_p)$  ▶ § 3.3
    if  $C_p(\mathbf{F}_p) \neq 0$  then
       $\Delta \lambda_p = \frac{-C_p - \tilde{\alpha} \lambda}{\sum_{i=1}^N \frac{1}{m_i} |\nabla_{\mathbf{x}_i} C_p(\mathbf{x})|^2 + \tilde{\alpha}}$  ▶ § 3.1
       $\lambda_p \leftarrow \lambda_p + \Delta \lambda_p$ 
       $\Delta \mathbf{v} = \frac{1}{\Delta t} \mathbf{M}^{-1} \nabla C_p(\mathbf{x})^T \Delta \lambda_p$ 
       $\mathbf{v} \leftarrow \mathbf{v} + \Delta \mathbf{v}$ 
    end if
  end for
  for all  $i \in \{C_i\}$  looping with colored Gauss-Seidel do
     $\Delta \mathbf{v} = \frac{1}{\Delta t} \mathbf{M}^{-1} \nabla C_i(\mathbf{x}^n + \Delta t \mathbf{v})^T \Delta \lambda_i$  (e.g., collision) ▶ § 4.4
     $\mathbf{v} \leftarrow \mathbf{v} + \Delta \mathbf{v}$ 
  end for
  end for
 $\mathbf{v}^{n+1} \leftarrow \mathbf{v}$ 
Perform XSPH smoothing of  $\mathbf{v}^{n+1}(\mathbf{x}^n)$  ▶ § 4.4
Update  $\mathbf{F}^{n+1}$  and apply constitutive models ▶ § 4.5
 $\mathbf{x}^{n+1} \leftarrow \mathbf{x}^n + \Delta t \mathbf{v}^{n+1}$ 
Note:  $\alpha = 1/V_p^0$  and  $\tilde{\alpha} = \alpha/\Delta t^2$  for each constraint.

```

(§ 4.2). 2^d colors are specified for eliminating dependencies between constraints in a d -dimensional simulation. We process all cells of the same color in parallel while constraints $C_p \in c_i$ corresponding to all particles in the same cell c_i are computed serially.

The efficiency of this implementation heavily depends on the average Particle Per Cell (PPC), as particles within the same cell are traversed sequentially. To optimize PPC and ensure an even particle distribution, we utilize Poisson disk sampling [Bridson 2007] during the initial particle placement.

4.4 XSPH and Position Correction

The goal of eXtended Smoothed Particle Hydrodynamics (XSPH) is to incorporate artificial viscosity for mitigating nonphysical oscillations in dynamics observed in SPH-based simulations, which is more observable when the material is stiff and the constraints become hard to solve. We follow Schechter and Bridson [2012]'s simpler XSPH-style noise damping after velocity update by blending in surrounding particle velocities in Ω^n :

$$\mathbf{v}_p^{n+1} \leftarrow \mathbf{v}_p^{n+1} + c \sum_b V_b^n (\mathbf{v}_b^{n+1} - \mathbf{v}_p^{n+1}) W_b(\mathbf{x}_p^n). \quad (20)$$

XSPH encourages smooth and coherent motion for inelastic materials in this paper. We use dimensionless $c = 0.01$ in all examples.

In particle-based simulations, including but not limited to FLIP [Brackbill and Ruppel 1986; Zhu and Bridson 2005] and APIC [Jiang et al. 2015], non-physical particle clumping and uneven particle

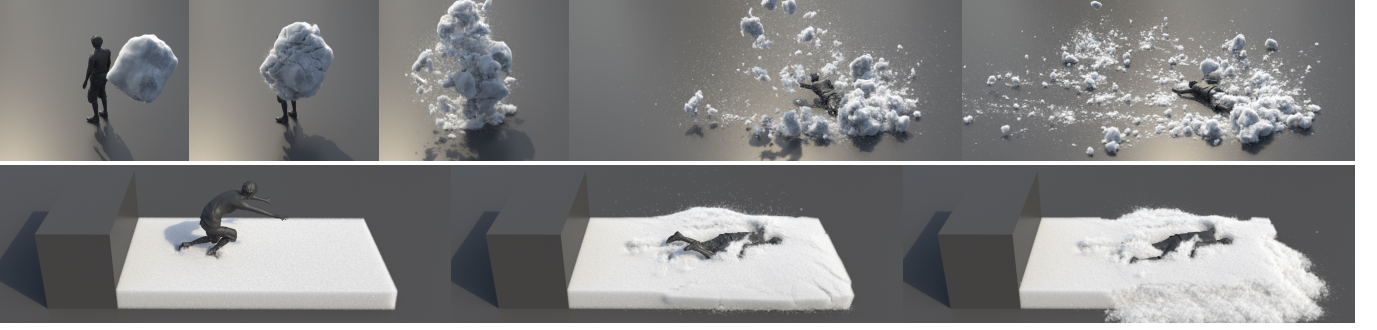


Fig. 12. **Hitman and Snow Dive.** We successfully reproduce realistic and complex snow behaviors, such as a snowball hitting a person (**top**) and a person falling into a snow ground (**bottom**), using NACC [Wolper et al. 2019] constitutive model.

distributions are common issues due to accumulation of advection errors. While MPM is insensitive to the problem due to its structural grid nature, it is crucial for pure particle-based methods like SPH and our approach to maintain reasonably even particle distributions. Without doing so can strongly impair simulation quality and convergence, particularly when material stiffness is high.

Various techniques in graphics have been proposed to address this by shifting particle positions [Ando et al. 2012; Ando and Tsununo 2011; Kugelstadt et al. 2019]. However, we point out that while these methods work well for fluids, they are problematic for updated Lagrangian simulations because such positional shifting is transparent to the evolution of deformation gradients, leading to discrepancy between the positions of points and their perceived deformations. Fortunately within XPBD we can directly adopt a point-point distance constraint [Macklin et al. 2014]

$$C(\mathbf{x}_p, \mathbf{x}_b) = \|\mathbf{x}_p - \mathbf{x}_b\|_2 - r + \epsilon \geq 0 \quad (21)$$

inside nonlinear iterations for all the neighborhood particle pairs. Here r represents the particle kernel radius and ϵ is a small gap threshold used to determine when corrective action is needed for nearby particle pairs. We set ϵ to $0.25r$.

4.5 Deformation Gradient Update

Strain variables within XPBD iterations are temporary. After arriving at the post-XSPH velocity \mathbf{v}^{n+1} , we update both the deformation gradient state and position state using the same velocity – an essential subtlety to maintain their consistency:

$$\mathbf{F}_p^{n+1} = \mathcal{Z} \left(\left(\mathbf{I} + \Delta t \frac{\partial \mathbf{v}^{n+1}}{\partial \mathbf{x}} (\mathbf{x}_p^n) \right) \mathbf{F}_p^n \right), \quad (22)$$

where inelastic return mapping is also applied to ensure the stored elastic deformation gradient is within the yield region.

5 RESULTS

Here we evaluate and benchmark our eXtended Position-based Inelasticity (XPBI) framework in terms of visual results against traditional XPBD and MPM methods, as detailed in § 5.1. Additionally, we present various demonstrations in § 5.2 that illustrate XPBI’s effective handling of diverse phenomena. We use Intel Core i9-14900KF CPU with 32GB memory and NVIDIA GeForce RTX 4090. We model

common inelastic materials including Cam-Clay (NACC) [Wolper et al. 2019] snow and fracture, Drucker-Prager [Klár et al. 2016; Tampubolon et al. 2017] sand, Von Mises [Li et al. 2022] plasticine and metal, and Herschel-Bulkley [Yue et al. 2015] foam.

5.1 Evaluation

Intuitive Parameters. We simulate sand collapsing with varying friction angles ϕ_f . Our method reproduces characteristic piling shapes. In Fig. 4, we compare viscoplastic, shear thinning, and shear thickening materials by only altering the Herschel-Bulkley power parameter h . Upon impact with a ground plane, the shear thickening material exhibits low flow rates under high stress, behaving elastically and bouncing off. Conversely, the shear thinning material flows immediately due to its higher flow rate. Similarly we can easily control the fluidity of viscoplastic goo (Fig. 10). A smaller μ gives a more fluid-like appearance, while a larger μ leads to more elastic behavior.

Comparisons to Vanilla XPBD and MPM. We compare XPBI sand with both vanilla XPBD [Macklin et al. 2016, 2014], which employs a point-wise friction model, and explicit MPM with Drucker-Prager plasticity [Klár et al. 2016]; see Fig. 13. This comparison includes simulations of *two sand blocks collide* (top) and *sand column collapse* (bottom). All methods apply a timestep of $\Delta t = 0.1$ ms, with identical initial sampling positions for all particles across the methods. The vanilla XPBD (left) approach fails to accurately replicate the correct friction angle upon sand settling. While both MPM (middle) and XPBI (right) successfully model the continuum behavior of sand, our

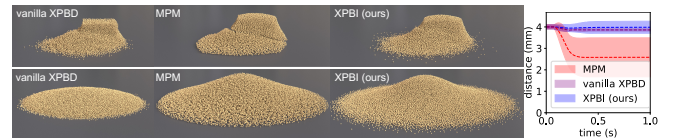


Fig. 13. **Vanilla XPBD v.s. MPM v.s. XPBI.** We simulate *two sand blocks collide* (top) and *sand column collapse* (bottom) with vanilla XPBD [Macklin et al. 2016, 2014] (left), MPM [Klár et al. 2016] (middle), and XPBI (right).

Table 2. Parameters and Statistics. We summarize the parameters and timing statistics, including maximum particle numbers, the Wendland kernel radius, the average total number of particle neighbors per substep, the average time per frame, the XPBD iterations per substep, and the time step size Δt for various demos described in § 5.2. Material-related parameters are detailed in the last two columns. The abbreviations are NACC for Non-Associated Cam-Clay [Wolper et al. 2019], DP for Drucker-Prager [Klár et al. 2016], VM for Von Mises [Li et al. 2022], and HB for Herschel-Bulkley [Yue et al. 2015]. In addition to the basic settings of the material (density ρ , Youngs Modulus E , and Poisson Ratio ν), we include model-specific parameters arranged as follows: 1) NACC: $(\rho, E, \nu, \alpha_0, \beta, \xi, M)$; 2) DP: $(\rho, E, \nu, \phi_f, c_0)$; 3) VM: (ρ, E, ν, σ_Y) ; and 4) HB: $(\rho, E, \nu, \sigma_Y, h, \eta)$. See references for detailed explanations of these parameters.

demo	particle #	radius	ave $\sum \mathcal{N}_p $	ave sec/frame	iter #	Δt_{frame}	Δt_{step}	material	material parameters
(Fig. 2) Noodles	1.18M	1/256	28.7M	46.3	10	1/40	1×10^{-4}	VM	$(1, 2 \times 10^4, 0.3, 76.9)$
(Fig. 3) Cloth	1.10M	1/512	19.9M	24.3	10	1/100	5×10^{-5}	HB	$(100, 14754, 0.475, 50, 1, 10)$
(Fig. 5) Camponotus	1.12M	1/1024	32.9M	37.3	10	1/100	4×10^{-5}	NACC	$(2, 2 \times 10^4, 0.35, -0.02, 0.5, 1, 2.36)$
(Fig. 7) Dam Breach	4.00M	1/384	156.2M	138.8	7	1/24	2.5×10^{-4}	DP	$(1, 400, 0.4, 30, 0.0007)$
(Fig. 8) Hourglass	1.01M	1/1024	17.0M	30.9	5	1/24	1×10^{-4}	DP	$(1, 3.537 \times 10^5, 0.3, 35, 0)$
(Fig. 12) Hitman	1.05M	1/512	32.5M	38.9	10	1/100	4×10^{-5}	NACC	$(4, 2 \times 10^4, 0.3, -0.005, 0.05, 30, 1.85)$
(Fig. 12) Snow Dive	2.48M	1/512	64.1M	78.2	5	1/100	4×10^{-5}	NACC	$(4, 1 \times 10^4, 0.3, -0.0005, 0.05, 30, 1.85)$
(Fig. 20) Wrist	20K	1/256	433.2K	0.015	5	1/100	2×10^{-4}	HB	$(100, 2250, 0.125, 10, 1, 10)$

method achieves a more uniform particle distribution, avoiding the sparsity, clumping, and artificial grid Δx -gap phenomena typically caused by MPM solvers. For a quantitative analysis, we also plotted the average distance between each particle and its nearest neighbor per frame, displayed on the far right of Fig. 13. Each particle was initially positioned at intervals equal to the particle radius. The average distance relative to the initial state in the MPM decreases rapidly post-collision, accompanied by an increase in the variance of the distance, whereas our method maintains both the relative distance and variance stably throughout the simulation, indicating a more consistent particle distribution. It is also noteworthy that our method aligns more closely with the approach of Yue et al. [2018] compared to MPM, opting for Discrete Element Method (DEM) to capture more discrete behaviors near the free surface.

Implicit Plasticity. We evaluate our fully implicit plasticity treatment by replacing it with a semi-implicit method, which only performs return mappings at the end of the time steps as in Stomakhin et al. [2013] § 4.5, while XPBD iterations only address elasticity. As shown in Fig. 9, the semi-implicit approach (right) can lead to severe artifacts. This occurs because the forces generated by stresses outside the yield surface cause the continuum to behave more like a purely elastic body. This artifact results from the semi-implicit method’s failure to account for plasticity during the XPBD solve, leading to an overestimation of the material’s resistance to tensile deformation. In contrast, our method (middle) fully incorporates plasticity in the XPBD iterations and avoids such artifacts.

Convergence. We study the convergence of our method using cantilever beams of varying stiffness, $E = 10^4$ Pa, 10^5 Pa, 10^6 Pa, respectively (Fig. 14). We set the density at 100 kg/m^3 and the timestep at $\Delta t = 5 \text{ ms}$. We also compare the relative residual errors of the Gauss-Seidel and Jacobi solvers in our method, as well as an implicit FEM ground truth, with respect to both iteration and time. XPBI with Gauss-Seidel can converge stably with a large timestep. In contrast, the Jacobi solver only converges with softer materials and struggles with high stiffness. This is consistent with observations about XPBD in prior work. Given that the materials discussed in our paper are predominantly very stiff, we opted for grid-colored

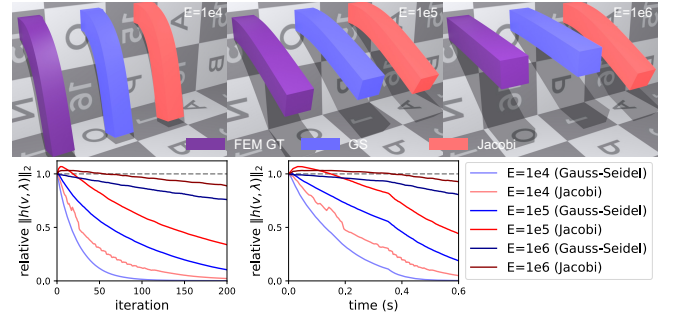


Fig. 14. Cantilever beams modeled with StVK constitutive model using both our method and FEM ground truth with varying stiffness (**top**). Relative residual errors $h(v, \lambda) = C(v) + \tilde{a}\lambda$ with respect to iteration (**bottom left**) and runtime (**bottom right**) for a single frame from the above examples.

Gauss-Seidel as our solver. Although using a large timestep is feasible with sufficient iterations, it becomes cost-inefficient if too many iterations are required. Thus, following Macklin et al. [2019], we employ a small timestep.

Position Correction. To validate the importance of position correction, we conducted a hydraulic test on a highly stiff aluminum wheel, as shown in Fig. 11. Without position correction, areas with significant deformation and stress suffer from gradient estimation errors due to uneven particle distribution, resulting in artificial fractures and eventually simulation instability. With position correction, however, we can reliably simulate high-stiffness materials under extensive deformation. This example also shows our capability in animating metal ductility using Von Mises plasticity.

In addition to the distance constraint, other position correction strategies can also be employed. For instance, Takahashi and Lin [2019] demonstrated that the density constraint is effective in addressing particle clustering while preserving volume. In Fig. 15, we quantitatively compare the distance and density constraints using the same setup as in Fig. 13. Although both constraints are effective in maintaining maximum density during simulation, the distance

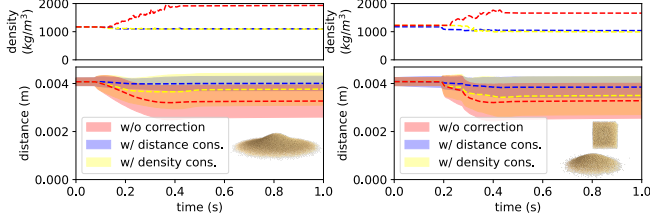


Fig. 15. Comparison of distance and density constraint. We plot the maximum density (**top**), the average distance to the nearest neighbor and respective standard deviations (**bottom**) for the settings described in Fig. 13.

constraint better resolves the distance between neighboring particles, improving both mean and variance, crucial for integration stability. We prefer the distance constraint for its simplicity.

Scalability. To demonstrate the scalability of our method, we simulate viscoplastic monsters hitting the ground using 8K, 56K, 400K, and 3M particles, respectively. We maintain a constant simulation time step of $\Delta t = 0.1$ ms, perform 10 iterations of XPBD per substep, and apply consistent material parameters across all simulations. Our method consistently replicates material behavior at varying resolutions, as depicted in Fig. 16. We measure and plot the computation time for each individual frame (left) alongside the average computation time per particle (right). The average computation times per particle for 8K, 56K, 400K, and 3M are 0.30 ms, 0.098 ms, 0.058 ms, and 0.037 ms, respectively. These results highlight strong scalability; as the number of particles increases, the colored Gauss-Seidel solver can more effectively exploit GPU resources, significantly reducing the overall computational overhead per particle.

Timing Breakdown. Fig. 17 illustrates the GPU computational cost breakdown for the *Hourglass* simulation example. In the breakdown, *Collision Detection* refers to the time spent on constructing the LBVH [Karras 2012] and querying for collision between point-triangle pairs. *Neighbor Search* covers the time taken to build the background grid and neighborhood list by querying adjacent cells (see § 4.2 for details). *Solve Inelasticity Constraints* involves our colored Gauss-Seidel solver for inelasticity constraints, including fixed-point implicit plasticity treatment. *Solve Other Constraints* accounts for the time spent on resolving all other constraints, such as point-triangle distance constraints for boundary conditions, position correction, as well as stretching, bending, and density constraints

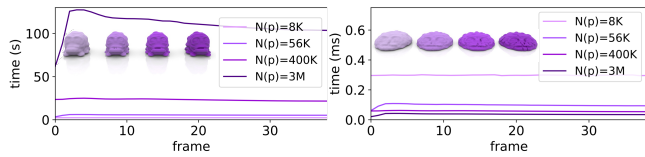


Fig. 16. We simulate viscoplastic monsters falling to the ground using varying numbers of particles. We plot the computation time for each frame for 8K, 56K, 400K, and 3M (**left**) particles, demonstrating consistent behaviors across different particle counts. We also plot the average cost per particle (**right**). The running overhead of our algorithm decreases significantly as the number of particles increases, showing strong superlinear scalability.

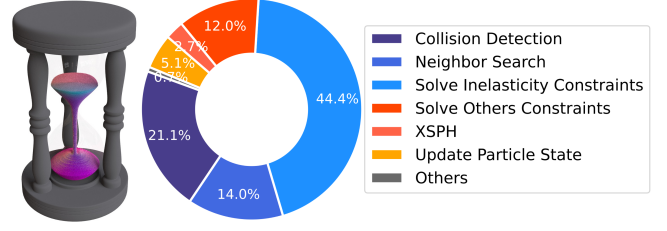


Fig. 17. A typical breakdown of the total computational cost of our framework. We take the *Hourglass* example (Fig. 8) for demonstration.

in other examples. *XSPH* and *Update Particle State* are detailed in § 4.4 and § 4.5, respectively. The majority of our framework’s computational time is spent on solving inelasticity constraints, while additional stability enhancements like *XSPH* and position correction contribute a relatively small overhead.

Choice of Time Step. While our method with colored GS solver can converge with a time step 5× larger, as noted by Macklin et al. [2019], smaller time steps are generally preferable due to the non-linear increase in GS iterations needed for convergence. However, we emphasize that reducing to just one iteration per time step is sub-optimal in our scenario, as shown in Fig. 17, where collision detection, neighbor search, *XSPH*, and particle state updates occur once per time step, accounting for about 1/3 of the total computation time. A timestep that is too small increases the overhead of these operations, with minimal benefit to GS convergence. We study the efficiency of different time step sizes by applying the same setting as in Fig. 14, this time fixing the residual error threshold ϵ_E and ensuring that each timestep converges under the given threshold, $\|h(v, \lambda)\|_2 \leq \epsilon_E$, with adaptive XPBD iterations. The ϵ_E values are chosen based on the residual errors observed when the cantilever beams exhibit visually identical behaviors to the FEM ground truth for each stiffness E , respectively. We measure the total XPBD iterations and runtime required relative to the timestep size for a 1-second simulation. As shown in Fig. 18, when stiffness is high, the total number of iterations required for convergence increases with the timestep size. Interestingly, when the timestep is sufficiently small, the total XPBD iterations required actually increases, as each timestep necessitates at least one iteration, and the runtime’s growth rate rises further due to the additional overhead per timestep. In practice, we select a Δt between 5×10^{-5} s and 2×10^{-4} s.

Comparison with Gissler et al. [2020]. Our method shares similarities with Gissler et al. [2020] in computing the velocity gradient

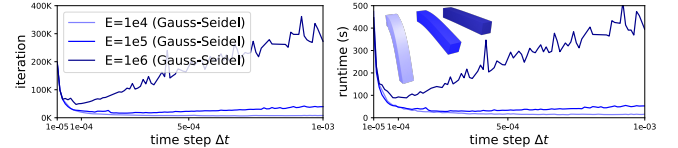


Fig. 18. Ablation on varying time step sizes. Total XPBD iterations (**left**) and runtime (**right**) required for all steps to converge to a fixed residual error for 1s simulation time with varying time step sizes.

and advecting the deformation gradient using SPH-based spatial discretization. However, Gissler et al. [2020] utilizes a Jacobi solver for the primal system, whereas we solve the dual formulation with a Lagrangian multiplier, enabling coupling with traditional PBD materials. A comprehensive discussion of the advantages/disadvantages of dual vs. primal formulations can be found at Macklin et al. [2020]. Most notably, as shown in Fig. 19, our approach to plasticity is distinct. We adopt the same snow constitutive model [2013] for both methods, with parameters: $\rho = 400 \text{ kg/m}^3$, $E = 5 \times 10^5 \text{ Pa}$, hardening coefficient $\xi = 10$, critical compression $\theta_c = 0.025$, and critical stretch $\theta_s = 0.0075$. We conducted simulations using timesteps of $\Delta t = 10^{-4} \text{ s}$ and 10^{-3} s . Gissler et al. [2020] employs a semi-implicit plasticity model with a single post-return-mapping projection per time step, akin to Stomakhin et al. [2013], making snow behavior timestep dependent due to this explicit plastic deformation update. In contrast, our method uses a fully implicit plasticity treatment, alternating between XPBD iteration and fixed-point iteration and producing consistent behaviors across different timestep sizes.

5.2 Demos

Complex materials with up to millions of particles, such as mud (Fig. 2, Fig. 7), viscoplastic paint (and its coupling with traditional XPBD cloth) (Fig. 3), brittle fracture (Fig. 5), sand (Fig. 8), and snow (Fig. 12) can be simulated with XPBI. The timing and parameters are summarized in Table. 2.

Real-time Interaction. The position-based method family is widely adopted in game and VR applications due to its real-time interactive capabilities [Barreiro et al. 2017; Jiang et al. 2024]. We further showcase our method in interactive applications where very small time steps are impractical. The convergence and stability of our approach enable interactive performance in moderately complex scenarios involving 20K particles. For this application, we employ the Jacobi solver due to its significant parallelism capabilities on GPUs for small-scale simulation. We use an Apple Vision Pro VR device and *VisionProTeleop* [Park and Agrawal 2024] to track hand motions and enable a virtual hand to interact with viscous fluids.

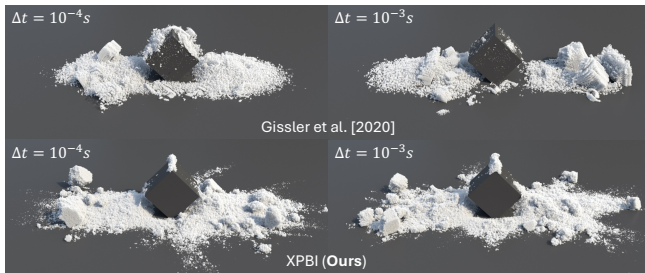


Fig. 19. Comparison with Gissler et al. [2020]. The semi-implicit plasticity approach in Gissler et al. [2020] (top) exhibits timestep-dependent behavior, whereas our method (bottom) demonstrates consistent behavior across different timestep sizes.



Fig. 20. **Real-time Vision Pro™ Interaction.** Interactive manipulation of a viscoelastic fluid, consisting of up to 20K particles, is simulated at 30fps.

6 DISCUSSION

In summary, XPBI is a novel updated Lagrangian enhancement for XPBD, enhancing its capability for simulating complex inelastic behaviors governed by continuum mechanics-based constitutive laws. Further incorporating an implicit plasticity treatment and stability enhancements, XPBI can be easily integrated into standard XPBD to open up its new simulation possibilities.

Given the high stiffness and detailed resolution of most scenes, the timestep is constrained by the relative low GS convergence and SPH CFL condition, which is related to the kernel’s support radius. We note that although our method falls under the category of implicit methods capable of handling highly stiff materials, additional damping models, such as XSPH or XPBD constraint damping, are still necessary to avoid jittering effects or stability issues.

While XPBI supports a broad range of material behaviors, Maxwell viscoelastic materials [Fang et al. 2019] necessitate more specialized treatment. Also, interactions between sand and water mixtures occur primarily at the material boundary. Simulating actual porous media [Tampubolon et al. 2017] and fluid sediment mixture [Gao et al. 2018] with proper momentum transfer are interesting future work. Another direction is to optimize parallelism for solving inelastic per-particle constraints. Although grid-colored Gauss-Seidel significantly improves performance over sequential iterations in large-scale simulations, it underperforms in small-scale cases on modern GPUs due to low utilization, obstructing many interactive rate experiments. A tailored real-time solver would be interesting.

ACKNOWLEDGMENTS

We thank the anonymous reviewers for their valuable feedback. We thank Siyu Ma for contributing to the demo design discussions. We acknowledge support from NSF (2301040, 2008915, 2244651, 2008564, 2153851, 2023780), UC-MRPI, Sony, Amazon, and TRI.

REFERENCES

- Nadine Abu Rumman, Prapanch Nair, Patric Müller, Loïc Barthe, and David Vanderhaeghe. 2020. ISPH-PBD: coupled simulation of incompressible fluids and deformable bodies. *The Visual Computer* 36, 5 (2020), 893–910.
- Iván Alduán and Miguel A Otaduy. 2011. SPH granular flow with friction and cohesion. In *Proceedings of the 2011 ACM SIGGRAPH/Eurographics symposium on computer animation*. 25–32.
- Ryoichi Ando, Nils Thurey, and Reiji Tsuruno. 2012. Preserving fluid sheets with adaptively sampled anisotropic particles. *IEEE Transactions on Visualization and Computer Graphics* 18, 8 (2012), 1202–1214.
- Ryoichi Ando and Reiji Tsuruno. 2011. A particle-based method for preserving fluid sheets. In *Proceedings of the 2011 ACM SIGGRAPH/Eurographics symposium on computer animation*. 7–16.
- Héctor Barreiro, Ignacio García-Fernández, Iván Alduán, and Miguel A Otaduy. 2017. Conformation constraints for efficient viscoelastic fluid simulation. *ACM Transactions on Graphics (TOG)* 36, 6 (2017), 1–11.
- Jan Bender, Dan Koschier, Patrick Charrier, and Daniel Weber. 2014. Position-based simulation of continuous materials. *Computers & Graphics* 44 (2014), 1–10.

- Jan Bender, Matthias Müller, and Miles Macklin. 2017. A survey on position based dynamics, 2017. In *Proceedings of the European Association for Computer Graphics: Tutorials*. 1–31.
- Javier Bonet and T-SL Lok. 1999. Variational and momentum preservation aspects of smooth particle hydrodynamic formulations. *Computer Methods in applied mechanics and engineering* 180, 1-2 (1999), 97–115.
- Sofien Bouaziz, Sebastian Martin, Tiantian Liu, Ladislav Kavan, and Mark Pauly. 2014. Projective dynamics: fusing constraint projections for fast simulation. *ACM Transactions on Graphics (TOG)* 33, 4 (2014), 1–11.
- Jeremiah U Brackbill and Hans M Ruppel. 1986. FLIP: A method for adaptively zoned, particle-in-cell calculations of fluid flows in two dimensions. *Journal of Computational physics* 65, 2 (1986), 314–343.
- Robert Bridson. 2007. Fast Poisson disk sampling in arbitrary dimensions. *SIGGRAPH sketches* 10, 1 (2007), 1.
- Wei Chen, Fei Zhu, Jing Zhao, Sheng Li, and Guoping Wang. 2018. Peridynamics-Based Fracture Animation for Elastoplastic Solids. In *Computer Graphics Forum*, Vol. 37. Wiley Online Library, 1219–124.
- Yizhou Chen, Yushan Han, Jingyu Chen, Shiqian Ma, Ronald Fedkiw, and Joseph Teran. 2023. Primal Extended Position Based Dynamics for Hyperelasticity. In *Proceedings of the 16th ACM SIGGRAPH Conference on Motion, Interaction and Games*. 1–10.
- Nuttapong Chentanez, Matthias Müller, and Miles Macklin. 2016. Real-time simulation of large elasto-plastic deformation with shape matching. In *Symposium on Computer Animation*. 159–167.
- Simon Clavet, Philippe Beaudoin, and Pierre Poulin. 2005. Particle-based viscoelastic fluid simulation. In *Proceedings of the 2005 ACM SIGGRAPH/Eurographics symposium on Computer animation*. 219–228.
- Gilles Daviet and Florence Bertails-Descoubes. 2016. A semi-implicit material point method for the continuum simulation of granular materials. *ACM Transactions on Graphics (TOG)* 35, 4 (2016), 1–13.
- Alban De Vaucorbeil, Vinh Phu Nguyen, Sina Sinaie, and Jian Ying Wu. 2020. Material point method after 25 years: theory, implementation, and applications. *Advances in applied mechanics* 53 (2020), 185–398.
- Daniel C. Drucker and William Prager. 1952. Soil mechanics and plastic analysis or limit design. *Quart. Appl. Math.* 10 (1952), 157–165.
- Michael Falkenstein, Ben Jones, Joshua A Levine, Tamar Shinar, and Adam W Bargteil. 2017. Reclustering for large plasticity in clustered shape matching. In *Proceedings of the 10th International Conference on Motion in Games*. 1–6.
- Yu Fang, Minchen Li, Ming Gao, and Chenfanfu Jiang. 2019. Silly rubber: an implicit material point method for simulating non-equilibrated viscoelastic and elastoplastic solids. *ACM Transactions on Graphics (TOG)* 38, 4 (2019), 1–13.
- Yun Fei, Christopher Batty, Eitan Grinspun, and Changxi Zheng. 2019. A multi-scale model for coupling strands with shear-dependent liquid. *ACM Transactions on Graphics (TOG)* 38, 6 (2019), 1–20.
- Yun Fei, Qi Guo, Rundong Wu, Li Huang, and Ming Gao. 2021. Revisiting integration in the material point method: a scheme for easier separation and less dissipation. *ACM Transactions on Graphics (TOG)* 40, 4 (2021), 1–16.
- Mihai Frăncu and Florica Moldoveanu. 2017. Unified Simulation of Rigid and Flexible Bodies Using Position Based Dynamics. In *Workshop on Virtual Reality Interaction and Physical Simulation*, Fabrice Jalilet and Florence Zara (Eds.). The Eurographics Association.
- Ming Gao, Andre Pradhana, Xuchen Han, Qi Guo, Grant Kot, Eftychios Sifakis, and Chenfanfu Jiang. 2018. Animating fluid sediment mixture in particle-laden flows. *ACM Transactions on Graphics (TOG)* 37, 4 (2018), 1–11.
- Ming Gao, Andre Pradhana, Tampubolon, Chenfanfu Jiang, and Eftychios Sifakis. 2017. An adaptive generalized interpolation material point method for simulating elastoplastic materials. *ACM Transactions on Graphics (TOG)* 36, 6 (2017), 1–12.
- Dan Gerszewski, Haimasree Bhattacharya, and Adam W Bargteil. 2009. A point-based method for animating elastoplastic solids. In *Proceedings of the 2009 ACM SIGGRAPH/Eurographics Symposium on Computer Animation*. 133–138.
- Christoph Gissler, Andreas Henne, Stefan Band, Andreas Peer, and Matthias Teschner. 2020. An implicit compressible SPH solver for snow simulation. *ACM Transactions on Graphics (TOG)* 39, 4 (2020), 36–1.
- Xiaowei He, Huamin Wang, and Enhua Wu. 2017. Projective peridynamics for modeling versatile elastoplastic materials. *IEEE transactions on visualization and computer graphics* 24, 9 (2017), 2589–2599.
- Jan Hegemann, Chenfanfu Jiang, Craig Schroeder, and Joseph M Teran. 2013. A level set method for ductile fracture. In *Proceedings of the 12th ACM SIGGRAPH/Eurographics Symposium on Computer Animation*. 193–201.
- Winslow H. Herschel and Ronald Bulkley. 1926. Konsistenzmessungen von Gummi-Benzollösungen. *Kolloid-Zeitschrift* 39 (1926), 291–300.
- Rama C Hoetzlein. 2014. Fast fixed-radius nearest neighbors: interactive million-particle fluids. In *GPU Technology Conference*, Vol. 18. 2.
- Yuanming Hu, Yu Fang, Ziheng Ge, Ziyin Qu, Yixin Zhu, Andre Pradhana, and Chenfanfu Jiang. 2018. A moving least squares material point method with displacement discontinuity and two-way rigid body coupling. *ACM Transactions on Graphics (TOG)* 37, 4 (2018), 1–14.
- Markus Ihmsens, Jens Orthmann, Barbara Solenthaler, Andreas Kolb, and Matthias Teschner. 2014. SPH fluids in computer graphics. (2014).
- Chenfanfu Jiang, Theodore Gast, and Joseph Teran. 2017. Anisotropic elastoplasticity for cloth, knit and hair frictional contact. *ACM Transactions on Graphics (TOG)* 36, 4 (2017), 1–14.
- Chenfanfu Jiang, Craig Schroeder, Andrew Selle, Joseph Teran, and Alexey Stomakhin. 2015. The affine particle-in-cell method. *ACM Transactions on Graphics (TOG)* 34, 4 (2015), 1–10.
- Chenfanfu Jiang, Craig Schroeder, Joseph Teran, Alexey Stomakhin, and Andrew Selle. 2016. The material point method for simulating continuum materials. In *ACM siggraph 2016 courses*. 1–52.
- Ying Jiang, Chang Yu, Tianyi Xie, Xuan Li, Yutao Feng, Huamin Wang, Minchen Li, Henry Lau, Feng Gao, Yin Yang, et al. 2024. VR-GS: a physical dynamics-aware interactive gaussian splatting system in virtual reality. In *ACM SIGGRAPH 2024 Conference Papers*. 1–1.
- Ben Jones, April Martin, Joshua A Levine, Tamar Shinar, and Adam W Bargteil. 2016. Ductile fracture for clustered shape matching. In *Proceedings of the 20th ACM SIGGRAPH Symposium on Interactive 3D Graphics and Games*. 65–70.
- Ben Jones, Stephen Ward, Ashok Jallepalli, Joseph Perenia, and Adam W Bargteil. 2014. Deformation embedding for point-based elastoplastic simulation. *ACM Transactions on Graphics (TOG)* 33, 2 (2014), 1–9.
- Tero Karras. 2012. Maximizing parallelism in the construction of BVHs, octrees, and k-d trees. In *Proceedings of the Fourth ACM SIGGRAPH/Eurographics Conference on High-Performance Graphics*. 33–37.
- Gergely Klár, Theodore Gast, Andre Pradhana, Chuyuan Fu, Craig Schroeder, Chenfanfu Jiang, and Joseph Teran. 2016. Drucker-prager elastoplasticity for sand animation. *ACM Trans. Graph.* 35, 4, Article 103 (jul 2016), 12 pages.
- Tassilo Kugelschadt, Andreas Longva, Nils Thuerey, and Jan Bender. 2019. Implicit density projection for volume conserving liquids. *IEEE Transactions on Visualization and Computer Graphics* 27, 4 (2019), 2385–2395.
- Xuan Li, Minchen Li, and Chenfanfu Jiang. 2022. Energetically consistent inelasticity for optimization time integration. *ACM Transactions on Graphics (TOG)* 41, 4 (2022), 1–16.
- Wing Kam Liu, Sukky Jun, and Yi Fei Zhang. 1995. Reproducing kernel particle methods. *International journal for numerical methods in fluids* 20, 8-9 (1995), 1081–1106.
- Miles Macklin, Kenny Erleben, Matthias Müller, Nuttapong Chentanez, Stefan Jeschke, and Tae-Yong Kim. 2020. Primal/dual descent methods for dynamics. In *Computer Graphics Forum*, Vol. 39. Wiley Online Library, 89–100.
- Miles Macklin and Matthias Müller. 2013. Position based fluids. *ACM Trans. Graph.* 32, 4, Article 104 (jul 2013), 12 pages.
- Miles Macklin, Matthias Müller, and Nuttapong Chentanez. 2016. XPBD: position-based simulation of compliant constrained dynamics. In *Proceedings of the 9th International Conference on Motion in Games (MIG '16)*. Association for Computing Machinery, New York, NY, USA, 49–54.
- Miles Macklin, Matthias Müller, Nuttapong Chentanez, and Tae-Yong Kim. 2014. Unified particle physics for real-time applications. *ACM Transactions on Graphics (TOG)* 33, 4 (2014), 1–12.
- Miles Macklin and Matthias Müller. 2021. A Constraint-based Formulation of Stable Neo-Hookean Materials. In *Motion, Interaction and Games*. 1–7.
- Miles Macklin, Kier Storey, Michelle Lu, Pierre Terdiman, Nuttapong Chentanez, Stefan Jeschke, and Matthias Müller. 2019. Small steps in physics simulation. In *Proceedings of the 18th Annual ACM SIGGRAPH/Eurographics Symposium on Computer Animation*. 1–7.
- R. v. Mises. 1913. Mechanik der festen Körper im plastisch- deformablen Zustand. *Nachrichten von der Gesellschaft der Wissenschaften zu Göttingen, Mathematisch-Physikalische Klasse* 1913 (1913), 582–592.
- Matthias Müller, Nuttapong Chentanez, Tae-Yong Kim, and Miles Macklin. 2015. Strain based dynamics. In *Proceedings of the ACM SIGGRAPH/Eurographics Symposium on Computer Animation* (Copenhagen, Denmark) (SCA '14). Eurographics Association, Goslar, DEU, 149–157.
- Matthias Müller, Bruno Heidelberger, Marcus Hennix, and John Ratcliff. 2007. Position based dynamics. *Journal of Visual Communication and Image Representation* 18, 2 (2007), 109–118.
- Matthias Müller, Richard Keiser, Andrew Nealen, Mark Pauly, Markus Gross, and Marc Alexa. 2004. Point based animation of elastic, plastic and melting objects. In *Proceedings of the 2004 ACM SIGGRAPH/Eurographics symposium on Computer animation*. 141–151.
- Matthias Müller, Tae Kim, and Nuttapong Chentanez. 2012. Fast Simulation of Inextensible Hair and Fur. *VRIPHYS 2012 - 9th Workshop on Virtual Reality Interactions and Physical Simulations*.
- Matthias Müller, Miles Macklin, Nuttapong Chentanez, Stefan Jeschke, and Tae-Yong Kim. 2020. Detailed Rigid Body Simulation with Extended Position Based Dynamics. *Computer Graphics Forum* 39, 8 (2020), 101–112.
- Younghyo Park and Pulkit Agrawal. 2024. Using Apple Vision Pro to Train and Control Robots. <https://github.com/Improbable-AI/VisionProTeleop>

- Steffen Plunder and Sara Merino-Aceituno. 2023. Convergence proof for first-order position-based dynamics: An efficient scheme for inequality constrained ODEs. *arXiv preprint arXiv:2310.01215* (2023).
- Ziyin Qu, Minchen Li, Fernando De Goes, and Chenfanfu Jiang. 2022. The power particle-in-cell method. *ACM Transactions on Graphics* 41, 4 (2022).
- Ziyin Qu, Minchen Li, Yin Yang, Chenfanfu Jiang, and Fernando De Goes. 2023. Power Plastics: A Hybrid Lagrangian/Eulerian Solver for Mesoscale Inelastic Flows. *ACM Transactions on Graphics (TOG)* 42, 6 (2023), 1–11.
- Daniel Ram, Theodore Gast, Chenfanfu Jiang, Craig Schroeder, Alexey Stomakhin, Joseph Teran, and Pirouz Kavehpour. 2015. A material point method for viscoelastic fluids, foams and sponges. In *Proceedings of the 14th ACM SIGGRAPH / Eurographics Symposium on Computer Animation* (Los Angeles, California) (SCA '15). Association for Computing Machinery, New York, NY, USA, 157–163.
- Hagit Schechter and Robert Bridson. 2012. Ghost SPH for animating water. *ACM Transactions on Graphics (TOG)* 31, 4 (2012), 1–8.
- Stewart A Silling. 2000. Reformulation of elasticity theory for discontinuities and long-range forces. *Journal of the Mechanics and Physics of Solids* 48, 1 (2000), 175–209.
- Breannan Smith, Fernando De Goes, and Theodore Kim. 2018. Stable neo-hookean flesh simulation. *ACM Transactions on Graphics (TOG)* 37, 2 (2018), 1–15.
- Alexey Stomakhin, Russell Howes, Craig A Schroeder, and Joseph M Teran. 2012. Energetically Consistent Invertible Elasticity. In *Symposium on Computer Animation*, Vol. 1.
- Alexey Stomakhin, Craig Schroeder, Lawrence Chai, Joseph Teran, and Andrew Selle. 2013. A material point method for snow simulation. *ACM Trans. Graph.* 32, 4, Article 102 (jul 2013), 10 pages.
- Alexey Stomakhin, Craig Schroeder, Chenfanfu Jiang, Lawrence Chai, Joseph Teran, and Andrew Selle. 2014. Augmented MPM for phase-change and varied materials. *ACM Trans. Graph.* 33, 4, Article 138 (jul 2014), 11 pages.
- Deborah Sulsky, Zhen Chen, and Howard L Schreyer. 1994. A particle method for history-dependent materials. *Computer methods in applied mechanics and engineering* 118, 1-2 (1994), 179–196.
- Tetsuya Takahashi, Yoshinori Dobashi, Issei Fujishiro, Tomoyuki Nishita, and Ming C Lin. 2015. Implicit formulation for SPH-based viscous fluids. In *Computer Graphics Forum*, Vol. 34. Wiley Online Library, 493–502.
- Tetsuya Takahashi and Ming C Lin. 2019. A geometrically consistent viscous fluid solver with two-way fluid-solid coupling. In *Computer Graphics Forum*, Vol. 38. Wiley Online Library, 49–58.
- Andre Pradhana Tampubolon, Theodore Gast, Gergely Klár, Chuyuan Fu, Joseph Teran, Chenfanfu Jiang, and Ken Museth. 2017. Multi-species simulation of porous sand and water mixtures. *ACM Trans. Graph.* 36, 4, Article 105 (jul 2017), 11 pages.
- Quoc-Minh Ton-That, Paul G Kry, and Sheldon Andrews. 2023. Parallel block Neo-Hookean XPBD using graph clustering. *Computers & Graphics* 110 (2023), 1–10.
- Maxime Tournier, Matthieu Nesme, Benjamin Gilles, and François Faure. 2015. Stable constrained dynamics. *ACM Trans. Graph.* 34, 4, Article 132 (jul 2015), 10 pages.
- Nobuyuki Umetani, Ryan Schmidt, and Jos Stam. 2015. Position-based elastic rods. In *Proceedings of the ACM SIGGRAPH/Eurographics Symposium on Computer Animation* (Copenhagen, Denmark) (SCA '14). Eurographics Association, Goslar, DEU, 21–30.
- Xinlei Wang, Minchen Li, Yu Fang, Xinxin Zhang, Ming Gao, Min Tang, Danny M. Kaufman, and Chenfanfu Jiang. 2020. Hierarchical Optimization Time Integration for CFL-Rate MPM Stepping. *ACM Trans. Graph.* 39, 3, Article 21 (apr 2020), 16 pages.
- Holger Wendland. 1995. Piecewise polynomial, positive definite and compactly supported radial functions of minimal degree. *Advances in computational Mathematics* 4 (1995), 389–396.
- Lukas Westhofen, Stefan Jeske, and Jan Bender. 2023. A comparison of linear consistent correction methods for first-order SPH derivatives. *Proceedings of the ACM on Computer Graphics and Interactive Techniques* 6, 3 (2023), 1–20.
- Joshuah Wolper, Yunuo Chen, Minchen Li, Yu Fang, Ziyin Qu, Jiecong Lu, Meggie Cheng, and Chenfanfu Jiang. 2020. Anisompm: Animating anisotropic damage mechanics. *ACM Transactions on Graphics (TOG)* 39, 4 (2020), 37–1.
- Joshuah Wolper, Yu Fang, Minchen Li, Jiecong Lu, Ming Gao, and Chenfanfu Jiang. 2019. CD-MPM: continuum damage material point methods for dynamic fracture animation. *ACM Trans. Graph.* 38, 4, Article 119 (jul 2019), 15 pages.
- Jingrui Xing, Liangwang Ruan, Bin Wang, Bo Zhu, and Baoquan Chen. 2022. Position-Based Surface Tension Flow. *ACM Trans. Graph.* 41, 6, Article 244 (nov 2022), 12 pages.
- Tao Yang, Jian Chang, Ming C Lin, Ralph R Martin, Jian J Zhang, and Shi-Min Hu. 2017. A unified particle system framework for multi-phase, multi-material visual simulations. *ACM Transactions on Graphics (TOG)* 36, 6 (2017), 1–13.
- Yonghao Yue, Breannan Smith, Christopher Batty, Changxi Zheng, and Eitan Grinspun. 2015. Continuum foam: A material point method for shear-dependent flows. *ACM Transactions on Graphics (TOG)* 34, 5 (2015), 1–20.
- Yonghao Yue, Breannan Smith, Peter Yichen Chen, Maytee Chantharayukhonthorn, Ken Kamrin, and Eitan Grinspun. 2018. Hybrid grains: Adaptive coupling of discrete and continuum simulations of granular media. *ACM Transactions on Graphics (TOG)* 37, 6 (2018), 1–19.
- Yongning Zhu and Robert Bridson. 2005. Animating sand as a fluid. *ACM Transactions on Graphics (TOG)* 24, 3 (2005), 965–972.